12th International Symposium on Turbulence and Shear Flow Phenomena (TSFP12)
Osaka, Japan (Online), July 19-22, 2022

NON-LINEARITIES IN TRANSITIONAL SHOCK WAVE / BOUNDARY LAYER INTERACTIONS

Mariadebora Mauriello
Aix-Marseille Univ, CNRS, IUSTI
Marseille, France
mariadebora.mauriello@univ-amu.fr

Lionel Larchevêque
Aix-Marseille Univ, CNRS, IUSTI
Marseille, France
lionel.larcheveque@univ-amu.fr

Pierre Dupont
Aix-Marseille Univ, CNRS, IUSTI
Marseille, France
pierre.dupont@univ-amu.fr

ABSTRACT

Large–eddy simulations (LES) of a transitional shock wave boundary layer interaction (TrSBLI) are carried out to investigate the origin of the low–frequency unsteadiness in an incident–reflecting shock configuration. The separated region is characterised by low–frequency breathing and is associated with a fluidic feedback originating from the vicinity of the reattachment point, in agreement with previous investigations. The non–linear spectral analysis reveals a quadratic coupling between the low–frequency feedback and the unstable modes developing within the separated shear layer. The chronological sequence of the phenomena is retrieved in the physical space through the bicorrelation statistical tool.

INTRODUCTION

Shock wave boundary layer interactions (SBLIs) have been the subject of extensive investigations in the last 70 years (Dolling, 2001). Much of the interest has been devoted to interactions between shock waves and turbulent boundary layers and the necessity of understanding such flows has motivated numerous experimental, numerical and theoretical studies. A large variety of geometrical configurations have been covered such as normal shock interactions, incident-reflecting interactions, compression corner, over–expanded nozzle, *etc.*, and investigations spanned a wide range of Mach and Reynolds numbers. The global organisation in terms of space and time dynamics have been depicted and the qualitative mean organisation of the flow is currently well understood. In the case of turbulent separated SBLIs, evidence showed that the interaction is highly unsteady with very low–frequency motions of the separated region (Dolling, 2001; Ganapathisubramani *et al.*, 2009; Dupont *et al.*, 2006). This phenomenon is often reported in the literature as *breathing* of the bubble and its origin is still under debate dividing the scientific community into different strands of thought. Multiple studies claim the upstream mechanism as a natural source of the low–frequency unsteadiness of the system such as broadband fluctuations (Touber & Sandham, 2011), or the existence of superstructures in the incoming turbulent boundary layer which are required to induce the flapping of the separated region (Ganapathisubramani *et al.*, 2009). Other authors propose to correlate this unsteadiness with the dynamics of the separated region (Wu & Pino Martín, 2008), or with a resonance mechanism in the interaction region (Pirozzoli & Grasso, 2006). Piponniau *et al.* (2009) developed a simple model to explain the low–frequency unsteadiness. It is based on the entrainment characteristics of the shear layer and relates the mass recharge within the separated bubble to the flapping dynamics occurring near to the reattachment point. However, a new consensus paved the way of uniting both upstream and downstream mechanism as contributors to the emergence of the low–frequency unsteadiness, but the effect of the incoming turbulent boundary layer diminishes for increasing interaction strengths (Clemens & Narayanaswamy, 2014). Less attention has been devoted to interactions between shock waves and an incoming laminar boundary layer and only recently the scientific community has taken steps in that direction. The TFAST project carried out both numerical (Sansica *et al.*, 2016; Larchevêque, 2016) and experimental (Diop *et al.*, 2019) studies on these transitional interactions. Their studies confirmed that unsteadiness comes up when transition to turbulence occurs. For example, Sansica *et al.* (2014) revealed that as the breakdown of the turbulence occurs, broadband disturbances travel upstream in the separated region of the boundary layer with a corresponding response near the separation point. Further, temporal measurements revealed several frequencies being amplified along the interaction with the low–frequency unsteadiness of the separation region being almost one order of magnitude higher than that found in the turbulent counterpart (Diop *et al.*, 2016). Sansica *et al.* (2016) demonstrated that the region of reattachment might be the origin of the low–frequency unsteadiness and Larchevêque (2016) showed that their amplitude vary significantly with the size of the separated region and the location of the transition to turbulence. However, all of these studies agree to associate the low–frequency unsteadiness with a feedback originating from the reattachment region, although a lot of open questions are left unanswered.

The present work aims to better characterise the physical origin of the low–frequency unsteadiness leveraging the non–linear spectral analysis, a tool that suits well when dealing with quadratic interactions.

Table 1. Flow parameters.

Mach	Re_{imp}	θ	L/δ^*_{imp}
1.68	0.65×10^6	4.96°	4.02

NUMERICAL SETUP

The datasets of the present numerical simulations are based on a transitional shock wave boundary layer interaction (TrSBLI) investigated in the experiments carried out in the TFAST project and performed at the IUSTI laboratory in Marseille (Diop *et al.*, 2019). The flow parameters of the incident-reflecting interaction are reported in table 1. Simulations were performed using the FLU3M code from ONERA. The code relies on a finite volume discretisation in space and an implicit Gear scheme for the temporal discretisation, both being second–order accurate. To minimise the numerical dissipation, the space scheme is modified by adding the dissipative part of the Roe scheme to a centered scheme in regions where strong compressibility/low vorticity occurs, as identified by means of Ducros sensor (Ducros *et al.*, 1999). The time integration is performed with a maximum Courant-Friedrichs-Lewy number of 11, and the non-linear system is solved through 7 sub-iterations resulting in a reduction of the residuals of more than three orders of magnitude in the laminar and transitional regions and about two orders of magnitude in the turbulent ones. The LES modeling is built from an implicit grid filtering coupled with an explicit subgrid modeling through the selective mixed-scale model. The reference meshes are $\Delta x^+ \lesssim 30$, $y_1^+ \lesssim 1.25$ and $\Delta z^+ \lesssim 15$ and the width of the computational domain is 7 times larger than the separation bubble height. Additional meshes refined by 40%, 20% and 25% in the x, y and z directions have been built in order to perform a grid convergence study. A mesh enlarged in the spanwise direction by 100% has also been tested. The wall is treated as adiabatic, and periodicity is used in the spanwise direction. Non-reflecting boundary conditions based on characteristics formulation are set at the inflow, outflow and upper boundaries. The inflow conditions are obtained by superimposing flow perturbations of very low amplitude and large bandwidth to the compressible Blasius profile by means of a compressible variant of the Synthetic Eddy Method (SEM). However, the amplitude of these perturbations were not known from the experiments. The strategy followed was to adjust them iteratively such that the final computations resulted in the same separation length as the experiments. The simulations were run long enough to encompass 70 cycles of the typical low–frequency unsteadiness allowing the extraction of spectral quantities.

VALIDATION

Computations have been compared to experimental measurements obtained through LDV technique and documented in Diop *et al.* (2019). The validation accounts for refined meshes in all of the directions as described in the previous section, and a mesh enlarged in the spanwise direction has also been validated. Figure 1 plots the mean streamwise velocity profiles at different streamwise locations. The streamwise coordinate is defined as the distance between the impingement location of the incident shock x_{imp} and the current location x and it is normalised by the incoming boundary layer thickness δ_{99}. The wall–normal coordinate is normalised by using the same reference length. All LES profiles collapse demonstrating that the procedure described in the previous section regarding the adjustment of the inflow perturbations amplitude is successful. In particular, experimental and numerical data show excellent agreement up to the apex of the recirculation bubble. Nonetheless, experiments tend to yield transition downstream of the apex. The transition phenomena occurs more abruptly over a shorter distance for the numerical data, resulting in quicker relaxation towards a canonical turbulent boundary layer downstream of the interaction region. It is unclear if this discrepancy is due to either the different physical nature of the perturbations in the incoming boundary layer or an alteration of the transition mechanism within the bubble due to the LES modelling. The fact that no difference is observed between the base computations and the ones relying on the refined meshes, even downstream of the apex, is an indication that the former hypothesis is more likely.

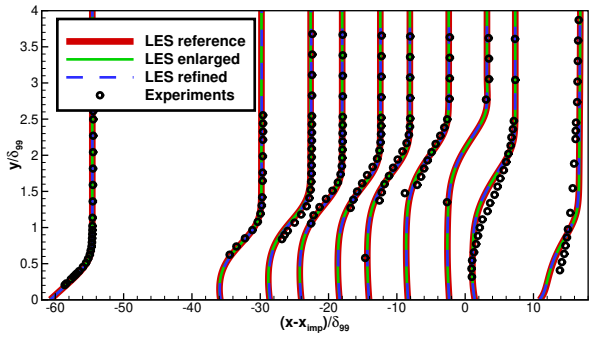

Figure 1. Comparison of the mean streamwise velocity profiles between experiments and computations at different streamwise locations.

LINEAR SPECTRAL ANALYSIS

The spectral analysis is considered to identify the key features of the shock motion and the characteristic temporal scales are extracted through spectral decomposition of wall pressure fluctuations.

Figure 2 shows the streamwise distributions of the pre-multiplied, normalised wall pressure spectrum. The horizontal axis displays the frequency normalised by the interaction length L_{int}, defined as the distance between the impingement location x_{imp} of the incident shock and the beginning of the interaction region x_{int}, and the free–stream velocity U_∞, corresponding to the Strouhal number $St_L = fL_{int}/U_\infty$. The vertical axis shows the streamwise evolution normalised by the interaction length L_{int}, as defined above. In this way the interaction region ranges from 0 to 1. The spectrum shows that the beginning of the interaction region, near $x^* = 0$, is dominated by power spectral density (PSD) content spreading at low frequencies, with typical Strouhal number of $St_L \simeq 0.055$. This value is close to the one found in the DNS by Sansica *et al.* (2016) and LES by Larchevêque (2016), but it is significantly lower than the $St_L \simeq 0.1$ value seen in the experiments by Diop *et al.* (2019). Conversely, the work of Bonne *et al.* (2019) yields an intermediate values of $St_L \simeq 0.08$. Such discrepancies in the low–frequency Strouhal numbers may be related to different physical forcing strategies of the incoming boundary layer/initial mixing layer adopted by the aforementioned works. Moving in the streamwise direction towards the impingement point $x^* = 1$, the typical frequency increases up to $St_L \simeq 0.6$. Once past this point, a spot of high PSD content emerges. It is localised in the region of the flow downstream

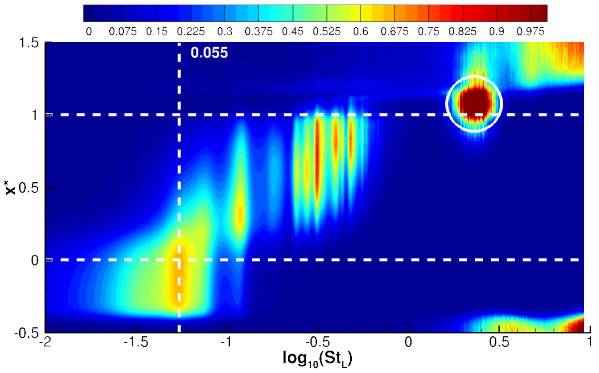

Figure 2. Streamwise evolution of the premultiplied, normalised wall pressure spectrum. White horizontal dashed lines mark separation ($x^* = 0$) and impingement ($x^* = 1$) locations while the vertical one correspond to the Strouhal number $St_L \simeq 0.055$. The white circle denotes the high PSD content associated with the transition and the breakdown of oblique instability modes.

the impingement point at $x^* \simeq 1.1$ and the associated Strouhal number is $St_L \simeq 2.1$ (see the white circle in figure 2). The presence of this high PSD spot has already been observed in the work of Larchevêque (2016) who investigated transitional SBLIs, but no evidence have been reported for the turbulent counterpart. Its presence is explained below. In the first part of the recirculating region, structures develop in the mixing layer zone and grow as they move downstream. After some distance, these structures are shed into the downstream flow, possibly leaving their trace at the wall. However, previous studies demonstrated that they remain at a certain distance from the wall, making the previous statement weak as the only explanation. Moreover, the mechanism just described is also common in turbulent interactions, where the emergence of such localised high PSD spot might be hidden by the turbulence from the incoming boundary layer. Therefore, other features have to be taken into account. The position $x^* \simeq 1.1$ is associated with the location where transition to turbulence occurs (results are not shown here). So, rather than a footprint of the mixing layer structures, it could represent the trace of the transition process. In addition, this spot could be related to the breakdown of oblique first–mode waves. In fact in this region, high disturbance amplitude is reached through linear growth that occurs along the mixing layer. Thus, oblique modes enter in the non–linear stage and transition soon follows. These instability modes originating from the initial mixing layer and propagating downstream to the reattachment point play a fundamental role in explaining the origin of low–frequency unsteadiness, as will be demonstrated in the next section.

From the previous analysis it emerges that the reattachment region is characterised by high–frequencies scales ($St_L \simeq 2.1$) associated with the breakdown of the oblique first–mode waves and transition. Conversely, the separation region is dominated by low–frequency scales ($St_L \simeq 0.05$) associated with the unsteadiness of the head shock. A question that arises now is: are the high–frequencies scales a local process or they affect all the other regions? To give insight into the question, a more deep investigation has been conducted by resorting to the phase information from the two–points spectrum. The cross–spectrum is a complex valued quantity defined as $S_{g_1,g_2}(f) = G_1(f)\,G_2^*(f)$, where $G_1(f)$ and $G_2(f)$ are the Fourier transforms of the time series $g_1(t)$ and $g_2(t)$ respectively, while $*$ denotes the complex conjugate. In this work, the streamwise momentum cross–spectrum has been computed and figure 3 shows the location of the sensors where ρu has been sampled. S_i correspond to the end of the ascending mixing layer ($S1$), the center of the descending mixing layer ($S2$) and three locations distributed on a horizontal plane fairly close to the wall, either upstream of, at, or downstream of the reattachment point ($S3$, $S4$ and $S5$ respectively). The reference point for the cross–spectrum is the position where the breakdown of the oblique modes occurs ($S1$) and all the possible linear links between streamwise momentum signals along a plane crossing sensors $S3$, $S4$ and $S5$ are obtained.

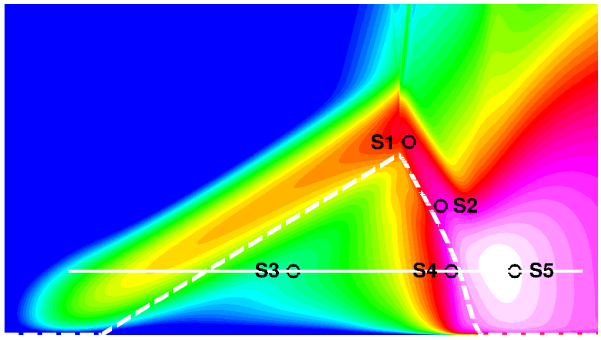

Figure 3. S_i indicates the location of the sensors used for the phase analysis as well as for the bispectral analysis. The contours show the exponentially–spaced filled isolevels of turbulent kinetic energy and the mean dividing streamline is indicated with white dashed line.

From the cross–spectrum, phase information is extracted for three regions, namely the separation point, inside the separation bubble and near the reattachment point, based on their characteristic Strouhal numbers, *i.e.* $St_L \simeq 0.055$, $0.11 < St_L < 0.33$ and $St_L \simeq 2.1$ respectively. Figure 4 plots the streamwise evolution of the normalised phase associated with ρu at the fixed aforementioned Strouhal numbers. Note that the normalisation of the streamwise coordinate is the same used for figure 2, but it is shifted from the wall. In this way $x^* = 0$ corresponds to the point where the plane considered for the analysis crosses the upstream mixing layer, while $x^* = 1$ is further downstream of the reattachment point (see horizontal straight white line in figure 3). Moreover, the phase data are normalised by the frequency and unwrapped so that jumps of 2π are removed, and shifted vertically such that phase is zero at the origin $x^* = 0$ of the reference frame. The inverse of the slope gives information regarding the phase velocity between the reference ρu at $S1$ and the selected streamwise momentum signals along the plane as well as the direction of travel. It is important to point out that the phase velocity is associated with a fixed frequency, but is contaminated by all the streamwise wavenumbers k_{x_i}. Not having selected a particular wavenumber, one can assume that rather than the phase velocity, what is observed is the average velocity at which the group of signals characterised by a given frequency is traveling, i.e. the group velocity V_g. By assuming $V_\Phi \sim V_g \sim U_c$ where U_c is the convection velocity, figure 4 provides the following information. For $St_L \simeq 2.1$, the phase increases linearly throughout the streamwise direction. The convection velocity is $U_c \simeq +0.5U_\infty$, meaning a motion from upstream towards downstream regions with respect to the location on the plane of sensor $S1$ indicated by the vertical dashed black line in the figure. However, for lower Strohual numbers an abrupt change in phase is observed at $x^* \simeq 0.95$. In particular, up to $x^* \simeq 0.95$,

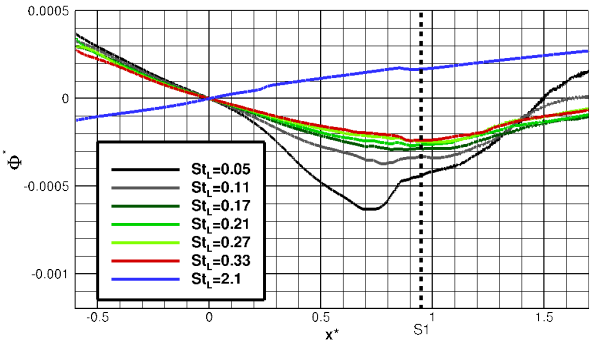

Figure 4. Streamwise evolution of the normalised phase associated with ρu for the Strouhal numbers *i.e.* $St_L \simeq 0.055$, $0.11 < St_L < 0.33$ and $St_L \simeq 2.1$. The vertical dashed line indicates the streamwise location shifted from the wall of sensor $S1$.

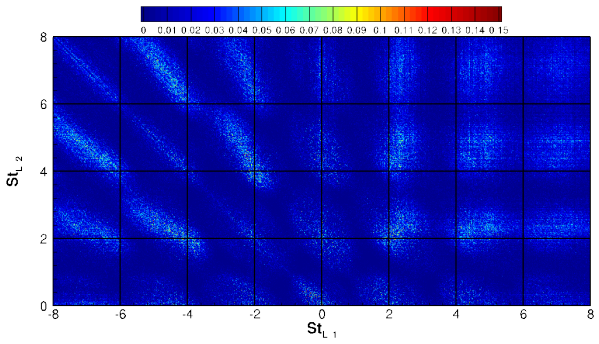

Figure 5. Bicoherence map between $S1 \times S1 \leftrightarrow S2$.

the phase decreases nearly linearly while it increases linearly everywhere else. Before the jump, upstream propagation velocities are found which correspond to $U_c \simeq -0.24U_\infty$ and $U_c \simeq -0.41U_\infty$ for the low and the medium frequencies respectively. After the jump, downstream propagation speeds are observed.

From this scenario it is possible to infer that the source of the slow–upstream motion is located at $x^* \simeq 0.95$, that at the wall corresponds to the position where the high PSD spot previously observed emerges (see figure 2). This high PSD content associated with the transition and oblique mode breakdown has a global effect. In fact, it affects the upstream region through a fluidic motion that starts from the position where the high PSD spot emerges and moves upstream at a convection velocity that decreases as the Strouhal number decreases. Moreover, the position $x^* \sim 0.95$ that corresponds at $x^* = 1.1$ at the wall, can be associated with the location of the source of the low–frequency unsteadiness.

NON–LINEAR ANALYSIS

Two–points spectral analysis revealed that the origin of the low–frequency breathing of the separation bubble corresponds with the location where the breakdown of the oblique modes emerges. Moreover, band-pass filtered pseudo-schlieren movies shows the occurrence of a fluidic feedback starting from the reattachment point for $St_L \lesssim 1$. It progressively restricts to a narrower low–frequency band while moving upstream in the separated region. From the movies, highly energetic fluctuations are also visible in the vicinity of the reattachment point for much higher frequencies. Therefore, multiple mechanisms are at play in this region, including transition and quadratic interactions that might involve different frequency bands. However, second–order statistics are limited to describing linear processes. To detect and quantify non–linearities in time series, higher–order statistics are required. In that context, bispectrum and bicoherence information are used to propose a scheme explaining how low-frequency motion appears near the reattachment point before being convected upstream, then inducing the breathing of the bubble. The region of the flow around the reattachment point is dominated by small–scale motions whose frequencies, as seen on the spot at $x^* \simeq 1.1$, $St_L \simeq 2.1$, are much higher than the low–frequency range associated with the upstream fluidic feedback. Because of the frequency difference, both phenomena cannot be linearly linked but they can be related through quadratic interactions. Such interactions can be highlighted in the spectral space from the bispectrum, which is a measure of the quadratic non–linearities at the bifrequency $(f_1,\ f_2)$ (Tynan *et al.*, 2001; Cui & Jacobi, 2021). One way to normalise the complex–valued bispectrum is the bicoherence between time series $g_1(t)$, $g_2(t)$ and $g_3(t)$, which reads:

$$Bic_{g_1,g_2,g_3}(f_1,f_2) = \frac{\left\|G_1(f_1)\,G_2(f_2)\,G_3^*(f_1+f_2)\right\|^2}{\left\|G_1(f_1)\,G_2(f_2)\right\|^2\,\left\|G_3(f_1+f_2)\right\|^2} \quad (1)$$

where $G(f)$ denotes the Fourier transform of the time series $g(t)$. A value of Bic_{g_1,g_2,g_3} that differs significantly from zero is associated with a (partial) phase relationship between $g_1 \times g_2$ and g_3 being stable over time, and it is indicative of possible non–linear energy exchange between the frequencies under consideration. In the present work, the analysed variable is the streamwise momentum ρu since it may experience quadratic interactions through the convective term of the Navier-Stokes momentum equation. The locations where ρu has been sampled has already been shown in figure 3. Figure 5 plots the bicoherence map between $S1 \times S1$ and $S2$ and the presence of strong bicoherence indicates those frequency modes that most strongly contribute towards the quadratic phase coupling (QPC). The linearly unstable modes develop in the ascending mixing layer and enter the non–linear regime near the apex of the bubble. Indeed, the positive quadrant of the bicoherence map is typical of a transitioning mixing layer. It displays an emerging direct turbulent cascade involving triadic interaction between frequency ranges being integer multiples of the original instability wave range at location $S1$, centered around $St_L \simeq 2$. On the contrary, quadrant defined by $St_{L_1} < 0$ and $St_{L_2} > 0$ displays a quadratic link towards lower–frequencies with $|St_{L_1}| \simeq |St_{L_2}|$. Spots of high values of bicoherence for very low values of Strouhal numbers are observed.

For triadic interactions between band-limited signals such as the ones centered around $St_L \simeq 2$, bicoherence is rather easy to analyse. However, such an analysis may become trickier for more broadband signals since a single frequency can be involved in multiple triadic interactions. One way to overcome this difficulty is to use the summed bicoherence (Tynan *et al.*, 2001), defined as:

$$\Sigma bic_{g_1,g_2,g_3}(f) = \frac{\sum_{|f_1+f_2|=f} \left\|G_1(f_1)\,G_2(f_2)\,G_3^*(f_1+f_2)\right\|^2}{\sum_{|f_1+f_2|=f} \left\|G_1(f_1)\,G_2(f_2)\right\|^2\,\left\|G_3(f_1+f_2)\right\|^2} \quad (2)$$

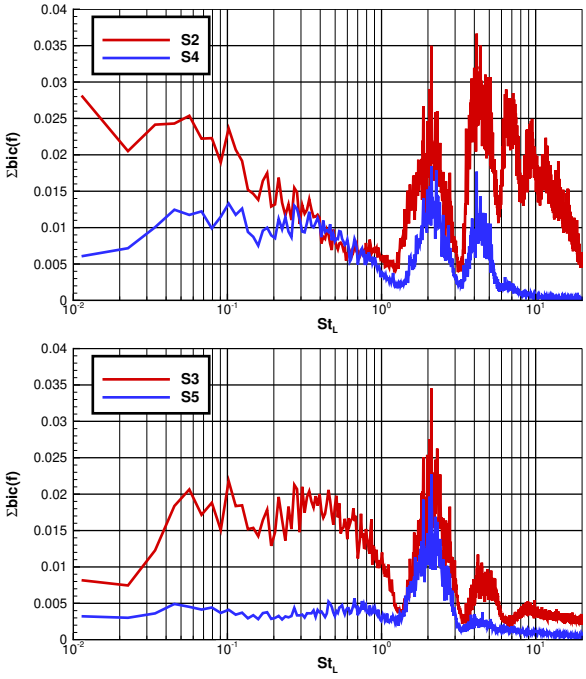

Figure 6. Summed bicoherence with $S1 \times S1$ for sensors located within the descending shear layer (upper panel) and near the wall, both upstream and downstream of the reattachment point (lower panel).

Summed bicoherence plots between the "source" signal $S1 \times S1$ and streamwise momentum at different locations are displayed in figure 6. Note that the low values associated with the summed bicoherence and reported in the y–axis are a consequence of the adopted normalisation (see equation 2). The cascade process for sensors $S2$ and $S4$ that are located at the center of, and near to the wall of the descending mixing layer is shown in the upper panel of figure 6. The energy transfer towards higher harmonics of the original instability wave at $St_L \simeq 2$ seen in the positive quadrant of figure 5, is mostly achieved when approaching the vicinity of the reattachment point (see sensor $S2$). Once the reattachment location is reached, the turbulence is close to be fully developed and only short–range triadic interactions are observed (see sensor $S4$). However, an energy transfer towards the low–frequency range takes place within the separation bubble, as sensor $S3$ shows in the lower panel of figure 6. For this range of low–frequency, the linear analysis revealed an upstream motion as pointed out with figure 4. No such process is identified downstream of the reattachment point as sensor $S5$ shows. It is worth noting that the relative energy content at low–frequency is increasing when moving upstream within the bubble. Based on these results, it can be postulated that the upstream low–frequency feedback is driven by quadratic interactions between high–frequency oblique modes found in the mixing layer developing over the separated region.

Bicoherence spectra convey information on the quadratic link between various regions of the flow, but do not provide any data regarding motion within these regions. However, information on the convective or stationary nature of the quadratic link can be recovered from the biphase spectrum using the same methodology developed for the cross–spectrum. The biphase spectrum correspond to the argument of the complex-valued bispectrum $G_1(f_1)\,G_2(f_2)\,G_3^*(f_1+f_2)$. For a given frequency pair (f_1, f_2), it is a measure of the phase difference between part of the g_3 series considered at frequency f_1+f_2 that is quadratically linked with part of the product between g_1 and g_2, considered at frequencies f_1 and f_2 respectively. The streamwise evolution of the biphase between the $S1 \times S1$ and sensors distributed over the horizontal line crossing sensors $S3$ to $S5$ is plotted in figure 7. High–frequency pairs whose sums correspond either to the various typical low-frequency Strouhal fluctuations identified in the separated region ($St_{L_3} < 1$) or to the oblique modes and their harmonics ($St_{L_3} \simeq \mathrm{n} \times 2.1, \mathrm{n} \in \mathbf{N}$) have been selected. Among the various frequency pairs of a given sum that have been computed, the three ones resulting in the largest bicoherence levels have been retained. In that sense, the streamwise phase evolution being plotted is representative of the strongest quadratic contributions to the low-frequency range. Comparison of figure 4 and figure 7 confirms that in the initial region of the interaction up to $x^* \simeq 0.95$ the phase evolution in both cases is very similar for the frequency range under consideration. As a consequence, the group velocity associated with the motion of the fluctuations quadratically linked with the oblique mode is roughly the same as the one found from the linear two–point analysis. This, coupled with the rather large values of bicoherence found in that region, confirms that the upstream–convected streamwise momentum fluctuations are for a large part induced by non–linear coupling with the mixing layer oblique modes. Since such an upstream motion has been associated with the low-frequency breathing of the separated region, it is therefore strongly suggested that the breathing is induced by non–linear beating in the vicinity of the reattachment point of the high–frequency oblique modes having developed within the mixing layer.

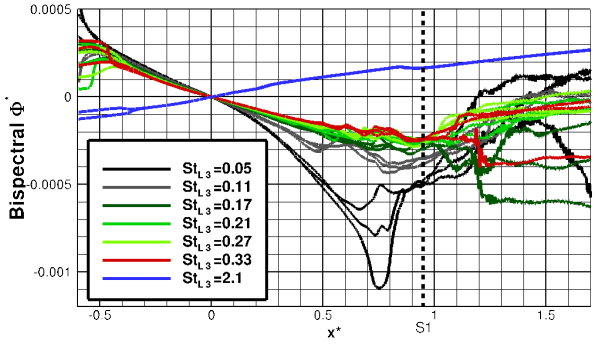

Figure 7. Streamwise evolution of the normalised biphase along the horizontal line crossing sensors S3 to S5. For each St_{L_3} spanning from low to high values, the three combinations resulting in the highest values of the bicoherence are plotted.

Up to now all the information have been extracted from the spectral space. However, the chronological sequence of the phenomena can be observed in the physical space by computing the inverse Fourier transform of the bispectrum, *i.e.* the bicorrelation that reads $R_{g_1,g_2,g_3}(\tau_1,\tau_2) = g_1(\tau_1)\,g_2(\tau_2)\,g_3^*(\tau_1+\tau_2)$. It is a measure of the time shift of the two time series $g_1(\tau_1)$ and $g_2(\tau_2)$ with respect to the third one $g_3(\tau_1+\tau_2)$. Figure 8 shows the bicorrelation map computed for the streamwise momentum with $S1 \times S1 \leftrightarrow S3$. The first two sensors are located in the region where the breakdown of the oblique modes occurs, $S1$, while the destination sensor is located in the separated region, $S3$. Note that also in this case the range of significant bicorrelation corresponds to a low values as a consequence of the normalisation. High bicorrelation values are observed for negative time delay suggesting that the non–linear coupling between the oblique unstable modes and

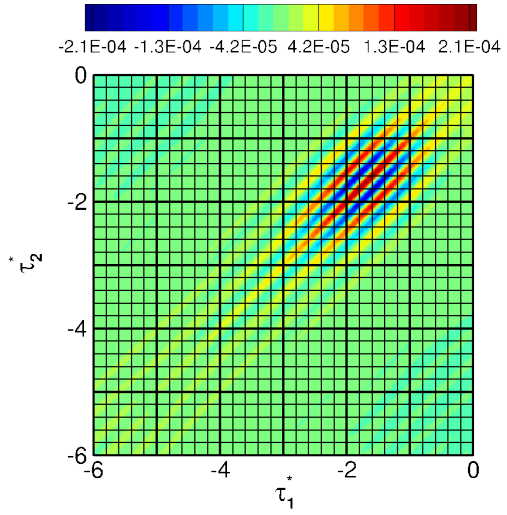

Figure 8. Bicorrelation map $S1 \times S1 \leftrightarrow S3$.

the low–upstream motion occurs after the apex of the separated region. Moreover the periodic pattern has been found to correspond with the period of the oblique mode being $\Delta\tau^* = St_L^{-1}$, with $St_L = 2.1$. This result confirms that the oblique modes and their harmonics are mostly involved in the non–linear interactions.

CONCLUSIONS

LES computations of a TrSBLI with separation have been carried out and compared with experimental databases from the TFAST project (Diop *et al.*, 2019). All computations have been validated resulting in a good agreement between experimental and numerical data. The higher–order statistical tools in the spectral space have been used to explore the linear and quadratic interactions responsible for the origin of the low–frequency unsteadiness. The two–points linear spectral analysis confirmed the occurrence of a slow–upstream convection motion originating from the vicinity of the reattachment point where a spot of high PSD content emerges. It has been shown that it globally affects the dynamics of the flow. The low–frequency range in the separated region was found to be significantly quadratically linked with the oblique mixing layer modes of much higher frequencies, as pointed out from bicoherence spectra. The biphase diagnostic then confirmed that such a long–range quadratic link is indeed related to the downstream-to-upstream fluidic feedback and from the bicorrelation analysis it is shown that is characterised by a negative time delay.

ACKNOWLEDGMENTS

This work was supported by TEAMAero Horizon 2020 research and innovation program under grant agreement 860909. This work was granted access to the HPC resources of CINES and IDRIS under the allocations A0022A01877, A0062A01877 and A0102A01877 made by GENCI.

REFERENCES

Bonne, N.and Brion, V., Garnier, E., Bur, R., Molton, P., Sipp, D. & Jacquin, L. 2019 Analysis of the two-dimensional dynamics of a mach 1.6 shock wave/transitional boundary layer interaction using a rans based resolvent approach. *Journal of Fluid Mechanics* **862**, 1166–1202.

Clemens, N. T. & Narayanaswamy, V. 2014 Low-frequency unsteadiness of shock wave/turbulent boundary layer interactions. *Annual Review of Fluid Mechanics* **46**, 469–492.

Cui, G. & Jacobi, I. 2021 Biphase as a diagnostic for scale interactions in wall-bounded turbulence. *Physical Review Fluids* **6**, 014604.

Diop, M., Piponniau, S. & Dupont, P. 2016 On the length and time scales of a laminar shock wave boundary layer interaction. In *54th AIAA Aerospace Sciences Meeting*.

Diop, M., Piponniau, S. & Dupont, P. 2019 High resolution lda measurements in transitional oblique shock wave boundary layer interaction. *Experiments in Fluids* **60**, 57.

Dolling, D. S. 2001 Fifty years of shock-wave/boundary-layer interaction research: What next? *AIAA Journal* **8**, 1517–1531.

Ducros, F., Ferrand, V., Nicoud, Weber, F. C., Darracq, D., Gacherieu, C. & Poinsot, T. 1999 Large-eddy simulation of the shock/turbulence interaction. *Journal of Computational Physics* **152**, 517–549.

Dupont, P., Haddad, C. & Debiève, J. F. 2006 Space and time organization in a shock-induced separated boundary layer. *Journal of Fluid Mechanics* **559**, 255–277.

Ganapathisubramani, B., Clemens, N. T. & S., Dolling D. 2009 Low-frequency dynamics of shock-induced separation in a compression ramp interaction. *Journal of Fluid Mechanics* **636**, 397–425.

Larchevêque, L. 2016 Low- and medium-frequency unsteadinesses in a transitional shock–boundary reflection with separation. *54th AIAA Aerospace Sciences Meeting* .

Piponniau, S., Dussage, J. P., Debiève, J. F. & P., Dupont 2009 A simple model for low-frequency unsteadiness in shock-induced separation. *Journal of Fluid Mechanics* **629**, 87–108.

Pirozzoli, S. & Grasso, F. 2006 Direct numerical simulation of impinging shock wave/turbulent boundary layer interaction at m=2.25. *Physics of Fluids* **065113**.

Sansica, A., Sandham, N. D. & Hu, Z. 2014 Forced response of a laminar shock-induced separation bubble. *Physics of Fluids* **26**, 093601.

Sansica, A., Sandham, N. D. & Hu, Z. 2016 Instability and low-frequency unsteadiness in a shock-induced laminar separation bubble. *Journal of Fluid Mechanics* **798**, 5–26.

Touber, E. & Sandham, N. D. 2011 Low-order stochastic modelling of low-frequency motions in reflected shock-wave/boundary-layer interactions. *Journal of Fluid Mechanics* **671**, 417–465.

Tynan, G. R., Moyer, R. A., Burin, M. J. & Holland, C. 2001 On the nonlinear turbulent dynamics of shear-flow decorrelation and zonal flow generation. *Physics of Plasmas* **8**, 2691–2699.

Wu, M. & Pino Martín, M. 2008 Analysis of shock motion in shockwave and turbulent boundary layer interaction using direct numerical simulation data. *Journal of Fluid Mechanics* **594**, 71–83.